Room-Temperature Spin-Orbit Torque from Topological Surface States

Hao Wu, Peng Zhang, Peng Deng, Qianqian Lan, Quanjun Pan, Seyed Armin Razavi, Xiaoyu Che, Li Huang, Bingqian Dai, Kin Wong, Xiufeng Han, and Kang L. Wang

Phys. Rev. Lett. **123**, 207205 — Published 15 November 2019

DOI: 10.1103/PhysRevLett.123.207205

Room-temperature spin-orbit torque from topological surface states

Hao Wu,[1,*] Peng Zhang,[1] Peng Deng,[1] Qianqian Lan,[2] Quanjun Pan,[1] Seyed Armin Razavi,[1] Xiaoyu Che,[1] Li Huang,[3] Bingqian Dai,[1] Kin Wong,[1] Xiufeng Han,[3] and Kang L. Wang[1,†]

[1]*Department of Electrical and Computer Engineering, and Department of Physics and Astronomy, University of California, Los Angeles, California 90095, United States*

[2]*Ernst Ruska-Centre for Microscopy and Spectroscopy with Electrons and Peter Grünberg Institute, Forschungszentrum Jülich, Jülich 52425, Germany*

[3]*Beijing National Laboratory for Condensed Matter Physics, Institute of Physics, Chinese Academy of Sciences, Beijing 100190, China*

Corresponding author. E-mail: [*]wuhaophysics@ucla.edu, [†]wang@ee.ucla.edu

Abstract:

Spin-momentum locked surface states in topological insulators (TIs) provide a promising route for achieving high spin-orbit torque (SOT) efficiency beyond the bulk spin-orbit coupling (SOC) in heavy metals (HMs). However, in previous works, there is a huge discrepancy among the quantitative SOTs from TIs in various systems determined by different methods. Here, we systematically study the SOT in the TI(HM)/Ti/CoFeB/MgO systems by the same method, and make a conclusive assessment of SOT efficiency for TIs and HMs. Our results demonstrate that TIs show more than one order of magnitude higher SOT efficiency than HMs even at room temperature, at the same time the switching current density as low as 5.2×10^5 A cm^{-2} is achieved with $(Bi_{1-x}Sb_x)_2Te_3$. Furthermore, we investigate the relationship between SOT efficiency and the position of Fermi level in $(Bi_{1-x}Sb_x)_2Te_3$, where the SOT efficiency is significantly enhanced near the Dirac point, with the most insulating bulk and conducting surface states, indicating the dominating SOT contribution from topological surface states. This work unambiguously demonstrates the ultrahigh SOT efficiency from topological surface states.

Main text:

Spin-orbit torque (SOT) [1-3] provides an efficient way to electrically manipulate the magnetic order. In general, SOT originates from the charge-spin conversion in materials with large spin-orbit coupling (SOC), which can be quantified as $\theta_{SH}=J_s^{3D}/J_e^{3D}$ or $q_{ICS}=J_s^{3D}/J_e^{2D}=\theta_{SH}/t_s$, where J_s^{3D} represents the 3-dimensional (3D) spin current density; J_e^{3D} and J_e^{2D} represent the 3D and 2-dimensional (2D) electric (charge) current density, respectively; and t_s represents the effective thickness of the SOC layer. SOT based on heavy metals (HMs) with bulk SOC has been widely studied, however, due to the limited θ_{SH} (typically around 0.1) [1, 4, 5], the switching current density J_c remains ultrahigh [6-8], therefore, improvement of SOT efficiency is still a major challenge for further reducing the power dissipation of SOT-based devices.

Spin-momentum locked surface states in topological insulators (TIs) are expected to be a promising candidate to break through the limited θ_{SH}, and previous works have reported the very large θ_{SH} (425) [9] and the SOT-induced magnetization switching [9-11] with TIs at low temperature. Recently, several works reported the room-temperature SOT switching by TIs [12-15], which is a crucial step towards practical applications. However, there exists a huge discrepancy among the reported θ_{SH} of TIs in various systems characterized by different methods, such as 0.047 in Bi_2Se_3/CoFeB [16] and 3.5 in Bi_2Se_3/NiFe [17] by the spin torque ferromagnetic resonance measurement, 0.16 in Bi_2Se_3/CoTb [12] and 0.40 in $(BiSb)_2Te_3$/CoTb [12] by the hysteresis loop shift measurement, 18.6 in Bi_2Se_3/CoFeB [13] by the planar

Hall measurement, and 52 in $Bi_{0.9}Sb_{0.1}$/MnGa [14] by the coercivity field shift measurement. Moreover, some groups argue that the bulk SOC [18, 19] and interfacial Rashba effect [20, 21] could also be involved in the SOT from TIs. Therefore, a conclusive study of SOT in TIs is in great need to clarify the actual spin current source and obtain the reliable SOT efficiency.

Here, we systematically investigate the SOT in a series of TIs and HMs, based on the similar TI(HM)/Ti/CoFeB/MgO heterostructures. We demonstrate the room-temperature SOT-induced magnetization switching, and the critical switching current density in $(Bi_{1-x}Sb_x)_2Te_3$ (5.2×10^5 A cm^{-2}) could be 1-2 orders of magnitude smaller than those in HMs. The charge-spin conversion efficiency θ_{SH} (or q_{ICS}) is obtained by the harmonic Hall method, which shows that TIs [θ_{SH} = 2.5 for $(Bi_{1-x}Sb_x)_2Te_3$] can break through the $\theta_{SH} < 1$ limitation in HMs. By engineering the band structure of $(Bi_{1-x}Sb_x)_2Te_3$, we find that the SOT strongly depends on the Fermi level position and reaches the maximum near the Dirac point with the most insulating bulk and conducting surface states, indicating the dominating SOT from topological surface states.

Figure 1(a) shows the schematic of SOT in the TI/Ti/CoFeB/MgO system. In topological surface states, the spin and momentum directions are locked [22-24], therefore, the electrical current flowing possess a net spin polarization. The spin current injection from the TI exerts a torque on the adjacent magnetic moment of CoFeB, and the anti-damping torque $\tau_{SOT} = \boldsymbol{m} \times (\boldsymbol{m} \times \boldsymbol{\sigma})$ can switch the magnetization at a sufficient current density, where $\boldsymbol{m}$ and $\boldsymbol{\sigma}$ represent the

magnetic and spin vectors, respectively. A constant external in-plane magnetic field H_{ext} is applied to break the mirror symmetry between $+M_z$ and $-M_z$ states and break the chiral domain walls to induce the domain wall expansion [25-27] for deterministic SOT switching. 6 quintuple-layers (QLs) TIs [$(Bi_{1-x}Sb_x)_2Te_3$, Bi_2Te_3 and SnTe] are grown on Al_2O_3(0001) substrates by using the molecular beam epitaxy method, and Ti(2 nm)/CoFeB(1.4 nm)/MgO(2 nm) multilayers are deposited by the magnetron sputtering method. The layer-by-layer growth of TIs is monitored by the reflection high-energy electron diffraction (RHEED). The sharp RHEED patterns show the high crystal quality and the flat surface, and the thickness of 6 QLs is determined by the periods of RHEED oscillations, as shown in Fig. 1(b). The non-magnetic interlayer Ti is used to provide the perpendicular magnetic anisotropy (PMA) of CoFeB. At the same time, the SOT contribution from Ti is negligible due to the extremely small θ_{SH} (0.0004) [28]. The films are patterned to 20 μm × 130 μm Hall bar devices. Figure 1(c) shows the M-H_z and R_{xy}-H_z loops in the $(Bi_{1-x}Sb_x)_2Te_3$/Ti/CoFeB/MgO sample, which show the strong perpendicular anisotropy (PMA) and the saturation magnetization M_s of 868 emu/cc. Figure 1(d) shows the high-angle annular dark field (HADDF) image and energy dispersive X-ray (EDX) mapping in the $(Bi_{1-x}Sb_x)_2Te_3$/Ti/CoFeB/MgO structure, indicating both the $(Bi_{1-x}Sb_x)_2Te_3$/Ti and Ti/CoFeB interfaces are clear and sharp, which promises the high interfacial spin transparency [29].

The SOT-induced magnetization switching is measured at room temperature in the TI(HM)/Ti/CoFeB/MgO structures with TIs of $(Bi_{1-x}Sb_x)_2Te_3$ [Fig. 2(a) and 2(b)], Bi_2Te_3 [Fig. 2(c) and 2(d)] and SnTe [Fig. 2(e) and 2(f)], and HMs of Ta [Fig. 2(g) and

2(h)], W [Fig. S4(a) and S4(b)] [30] and Pt [Fig. S4(c) and S4(d)] [30]. The non-volatile SOT switching is measured by the pulsed current, where a 1-ms writing current pulse J_W is applied to provide the SOT, followed by another 1-ms reading current pulse J_R to read the R_{xy}, where the reversed switching chirality at ±100 Oe H_x shows the typical SOT characteristic. It is known that the switching current density J_c depends on the magnitude of the in-plane magnetic field H_x [33], and 100 Oe is enough to overcome the Dzyaloshinskii–Moriya interaction (DMI) and obtain the saturation (minimum) value of J_c in our systems. We calculate the current density J_e in TIs and HMs by the parallel circuit model. Compared to HMs (Ta, W and Pt), the switching current density J_c of TIs [$(Bi_{1-x}Sb_x)_2Te_3$, Bi_2Te_3 and SnTe] is much smaller. In $(Bi_{1-x}Sb_x)_2Te_3$, J_c of 5.2×10^5 A cm^{-2} is 1-2 orders of magnitude smaller than the typical value of 10^6 - 10^7 A cm^{-2} in HMs, which indicates the high charge-spin conversion efficiency in topological surface states. It is worth noting that the chirality of SOT switching in Bi_2Te_3 is opposite to that in $(Bi_{1-x}Sb_x)_2Te_3$ and SnTe, which comes from the bulk states contribution, as to be discussed later.

The harmonic Hall method [34, 35] is employed to quantify the SOT: when we apply an ac current density $J_e = J_0 \sin \omega t$, the SOT induced effective field $H_{SOT} = H_0 \sin \omega t$ exerts the oscillation of $\boldsymbol{M}$, which contributes to the 2ω Hall signal $R_{xy}^{2\omega}$. When H_x is larger than the magnetic anisotropy field H_k, $R_{xy}^{2\omega}$ can be written as:

$$R_{xy}^{2\omega} = \frac{R_A}{2}\frac{H_{DL}}{|H_x| - H_k} + R_P\frac{H_{FL}}{|H_x|} + R_{SSE+ANE}\frac{H_x}{|H_x|} + R_{offset} \quad (1)$$

where H_{DL} and H_{FL} represent the effective field from the damping-like [$\boldsymbol{m}\times(\boldsymbol{m}\times\boldsymbol{\sigma})$] and field-like ($\boldsymbol{m}\times\boldsymbol{\sigma}$) torques, respectively; R_A and R_P represent the anomalous Hall (AHE) and planar Hall (PHE) resistances [36], respectively; $R_{SSE+ANE}$ is the thermal contribution [37, 38], and R_{offset} is the offset signal.

The harmonic Hall signals $R_{xy}^{1\omega}$ and $R_{xy}^{2\omega}$ as a function of H_x are measured in the TI(HM)/Ti/CoFeB/MgO structures with TIs of $(Bi_{1-x}Sb_x)_2Te_3$ [Fig. 3(a) and 3(b)], Bi_2Te_3 [Fig. 3(c) and 3(d)] and SnTe [Fig. 3(e) and 3(f)], and HMs of Ta [Fig. 3(g) and 3(h)], W [Fig. S5(a) and S5(b)] [30] and Pt [Fig. S5(c) and S5(d)] [30]. By fitting the $R_{xy}^{2\omega}$-H_x curve with equation (1), we can obtain H_{DL} and $\chi_{SOT}=H_{DL}/J_e$. θ_{SH} is calculated by $\theta_{SH}=\left(2|e|M_s t_F/\hbar\right)\times\chi_{SOT}$, where e is the electron charge, t_F is the magnetic film thickness, and $\hbar$ is the reduced Planck constant. The polar magneto optic Kerr effect (MOKE) is also employed to measure χ_{SOT} [30], where χ_{SOT} obtained by the optical MOKE method is consistent with that from the harmonic Hall method, indicating the asymmetric magnon scattering [10] contribution is negligible. Moreover, due to the shunting effect and the small magnetic field we use, the second harmonic contribution of the bilinear magnetoelectric resistance from TIs themselves is also negligible [39].

Table 1 summaries $|J_c|$, $|\chi_{SOT}|$, $|\theta_{SH}|$, magnetic anisotropy field H_k, electrical conductivity σ_c, t_s, $|q_{ICS}|$ and power dissipation density P_D in TIs [$(Bi_{1-x}Sb_x)_2Te_3$, Bi_2Te_3 and SnTe] and HMs (Ta, W and Pt). The t_s in TIs is estimated from the half hybridization thickness of the top and bottom surface states [40], and in HMs is obtained by the spin diffusion length [41]. $|\theta_{SH}|$ and $|q_{ICS}|$ in $(Bi_{1-x}Sb_x)_2Te_3$ are more

than one order of magnitude larger than those in HMs, which is consistent with the ultralow J_c of 5.2 × 10^5 A cm^{-2} (10^6 - 10^7 A cm^{-2} in HMs). P_D is proportional to J_c^2/σ_c, by considering the smaller σ_c in $(Bi_{1-x}Sb_x)_2Te_3$ that increases the ohmic loss, P_D in $(Bi_{1-x}Sb_x)_2Te_3$ (0.15 × 10^{16} W m^{-3}) is still much reduced compared to HMs (0.35 ~ 12.8 × 10^{16} W m^{-3}).

The sign of θ_{SH} in $(Bi_{1-x}Sb_x)_2Te_3$ and SnTe is the same with that in Ta (negative), indicating the bottom surface states of TIs dominate the SOT, because the work function difference in top TI/metal interface shifts the Fermi level away from the surface states and thus smears out the helical spin structure in the top surface [42]. This can also be proven by the TI thickness dependence [30] and voltage gating measurements [11]. The signs of θ_{SH} and q_{ICS} in Bi_2Te_3 are opposite to those in $(Bi_{1-x}Sb_x)_2Te_3$ and SnTe, indicating their different SOT origins: bulk states in Bi_2Te_3 and surface states in $(Bi_{1-x}Sb_x)_2Te_3$ and SnTe. It is worth noting that $|\theta_{SH}|$ and $|q_{ICS}|$ are enhanced when the topological surface states dominate as in $(Bi_{1-x}Sb_x)_2Te_3$ and SnTe, which contributes to a smaller σ_c, while the dominating bulk states in Bi_2Te_3 contribute to a much reduced $|\theta_{SH}|$ and $|q_{ICS}|$.

Tuning the band structure of TIs to eliminate the bulk states contribution is very crucial for the intrinsic quantum transport of topological surface states [43, 44]. Moreover, SOC from bulk states in TIs could also contribute to the SOT. Therefore, tuning the Fermi level of TIs by band engineering and investigating the Fermi level dependence are very essential to figure out the dominating SOT contribution [45]. We tune the Fermi level E_F by changing the Sb ratios (x) in $(Bi_{1-x}Sb_x)_2Te_3$ [46], as shown

in Fig. 4(a). From the 2-dimensional carrier density $|n_{2D}|$ and resistivity ρ_{xx} as a function of Sb ratios x in Fig. 4(b), we can obtain that E_F starts from the bulk conduction band (x = 0, n-type), to the topological surface band (x = 0.7-0.93, n-type), and then to the bulk valence band (x = 1.0, p-type). E_F is close to the Dirac point at x = 0.85 and 0.93, which shows the ideal topological properties with much insulating bulk.

Then we investigate the SOT in these samples [$(Bi_{1-x}Sb_x)_2Te_3$/Ti/CoFeB/MgO] with varied E_F, and the details are shown in the Supplemental Material [30]. J_c and χ_{SOT} as a function of Sb ratios are shown in Fig. 4(c), which show that $(Bi_{1-x}Sb_x)_2Te_3$ with much insulating bulk and conducting surface states contribute to larger χ_{SOT} and smaller J_c. By comparing the results of x = 0 (E_F in the bulk conduction band), x = 0.7-0.93 (E_F in the topological surface band), and x = 1.0 (E_F in the bulk valence band), we obtain that χ_{SOT} from topological surface states can be more than one order of magnitude larger than that from the bulk states. χ_{SOT} reaches the maximum value (67.6×10^{-6} Oe A^{-1} cm^2) near the Dirac point (x = 0.93), while J_c is significantly reduced (5.2×10^5 A cm^{-2}) at the same time. In our work, the main purpose of tuning the Fermi level near the Dirac point is to minimize the bulk states contribution, and the most dominating topological surface states contribute to the maximal SOT.

In this work, we systematically investigate the SOT from TIs and HMs in TI(HM)/Ti/CoFeB/MgO systems. One of the main purposes of our work is to resolve the huge discrepancy (θ_{SH} from 0.047 to 425) of SOT from TIs in different systems characterized by different methods, and to make a conclusive comparison between TIs

and HMs. By using the same method and the same structures, our results clearly show that TIs have much higher SOT and energy efficiency than HMs even at room temperature. By tuning the Fermi level of TIs, we show that the SOT is significantly enhanced when the topological surface states dominate, while the bulk states contribute to a very small SOT. These findings indicate that the discrepancy of SOT efficiency from TIs in previous works comes from the different contributions from the bulk and topological surface states. Our work unambiguously demonstrates the giant SOT from topological surface states at room temperature.

Acknowledgements:

This work is supported by the NSF Award No. 1611570, the Nanosystems Engineering Research Center for Translational Applications of Nanoscale Multiferroic Systems (TANMS), the U.S. Army Research Office MURI program under Grants No. W911NF-16-1-0472 and No. W911NF-15-1-10561, and the Spins and Heat in Nanoscale Electronic Systems (SHINES) Center funded by the US Department of Energy (DOE), under Award No. DE-SC0012670. We are also grateful to the support from the Function Accelerated nanoMaterial Engineering (FAME) Center, and a Semiconductor Research Corporation (SRC) program sponsored by Microelectronics Advanced Research Corporation (MARCO) and Defense Advanced Research Projects Agency (DARPA). X.F.H acknowledges the National Key Research and Development Program of China [Grant No. 2017YFA0206200], and the NSFC of China [Grant No.11434014].

Figures:

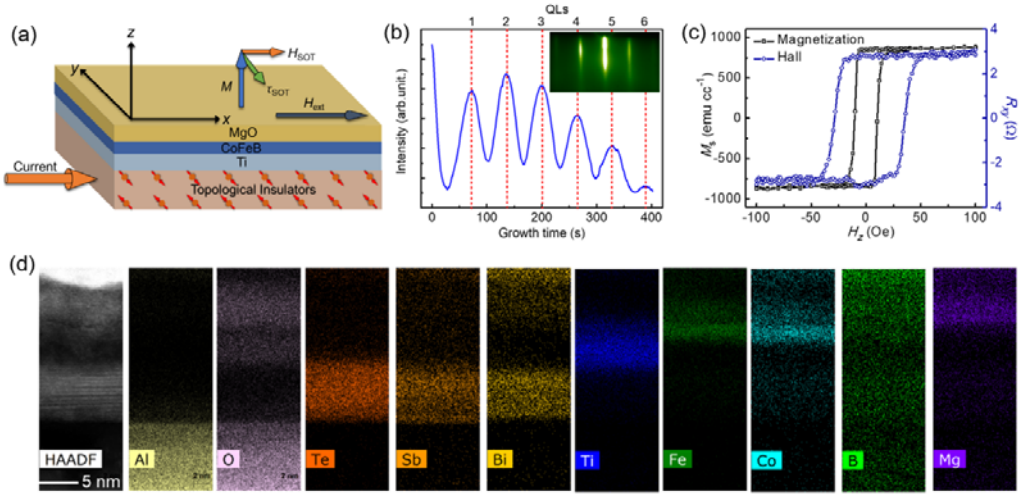

FIG. 1. (a) Schematic of SOT-induced magnetization switching in TI/Ti/CoFeB/MgO heterostructures. The electrical current flowing in topological surface states is spin-polarized by the spin-momentum locking, and this spin accumulation exerts a spin torque τ_{SOT} on the adjacent magnetic moment M of CoFeB. (b) The RHEED oscillations show the layer-by-layer growth mode of $(Bi_{1-x}Sb_x)_2Te_3$. (c) Saturation magnetization M_s and Hall resistance R_{xy} as a function of H_z. (d) High-angle annular dark field image and energy dispersive X-ray mapping in the $(Bi_{1-x}Sb_x)_2Te_3$/Ti/CoFeB/MgO heterostructure.

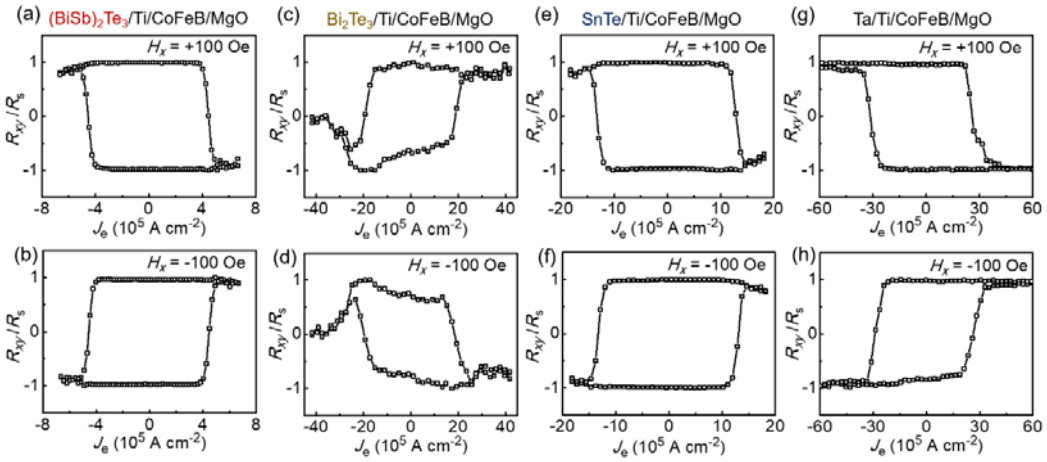

FIG. 2. Room temperature SOT-induced magnetization switching in TI(HM)/Ti/CoFeB/MgO heterostructures. The R_{xy}-J_e curves are shown in the figures for the TI(HM)/Ti/CoFeB/MgO heterostructures with $(Bi_{1-x}Sb_x)_2Te_3$ (a, b), Bi_2Te_3 (c, d), SnTe (e, f) and Ta (g, h), respectively, where the in-plane magnetic field H_x of ± 100 Oe is applied for the deterministic SOT switching, respectively.

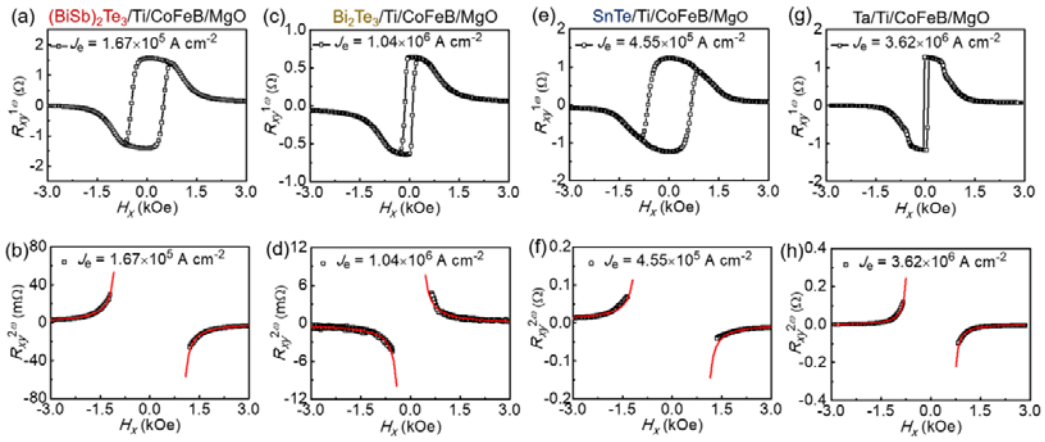

FIG. 3. Harmonic Hall measurement in TI(HM)/Ti/CoFeB/MgO heterostructures. The 1ω and 2ω harmonic Hall resistances ($R_{xy}^{1\omega}$ and $R_{xy}^{2\omega}$) as a function of in-plane magnetic field H_x for the TI(HM)/Ti/CoFeB/MgO heterostructures with $(Bi_{1-x}Sb_x)_2Te_3$ (a, b), Bi_2Te_3 (c, d), SnTe(e, f) and Ta (g, h), respectively.

Table 1 | Room-temperature $|J_c|$, $|\chi_{SOT}|$, $|\theta_{SH}|$, H_k, σ_c, t_s, $|q_{ICS}|$ and P_D of TIs and HMs in this work

	$\lvert J_c\rvert$ (10^6 A cm^{-2})	$\lvert\chi_{SOT}\rvert$ (10^{-6} Oe A^{-1} cm^2)	$\lvert\theta_{SH}\rvert$	H_k (kOe)	σ_c (10^4 Ω^{-1} m^{-1})	t_s (nm)	$\lvert q_{ICS}\rvert$ (nm^{-1})	P_D (10^{16} W m^{-3})
$(BiSb)_2Te_3$	0.52	67.6	2.50	2.24	1.83	1.5	1.67	0.15
Bi_2Te_3	2.43	2.20	0.08	2.06	15.0	1.5	0.05	0.39
SnTe	1.46	38.1	1.41	2.18	5.45	1.5	0.94	0.39
Ta	3.44	4.94	0.19	2.10	34.3	1.9	0.10	0.35
W	4.57	3.65	0.13	1.88	38.8	2.1	0.06	0.54
Pt	33.5	0.30	0.01	1.84	87.2	7.3	0.001	12.8

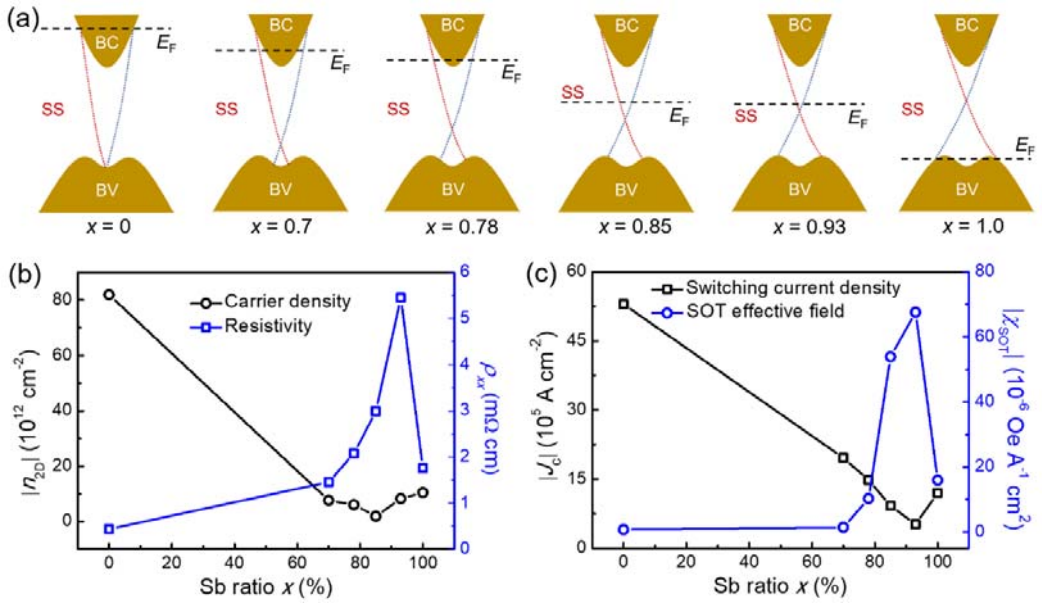

FIG. 4. (a) Schematic of the Fermi level positions for different Sb ratios (x = 0, 0.7, 0.78, 0.85, 0.93, 1.0) of $(Bi_{1-x}Sb_x)_2Te_3$, which are estimated from the 2-dimensional (2D) carrier density $|n_{2D}|$ and resistivity ρ_{xx}. (b) $|n_{2D}|$ and ρ_{xx} as a function of Sb ratios in $(Bi_{1-x}Sb_x)_2Te_3$. (c) Switching current density $|J_c|$ and SOT-induced effective field $|\chi_{SOT}|$ as a function of Sb ratios.

References:

[1] L. Liu, C.-F. Pai, Y. Li, H. W. Tseng, D. C. Ralph and R. A. Buhrman, Science **336** (6081), 555-558 (2012).

[2] I. M. Miron, K. Garello, G. Gaudin, P.-J. Zermatten, M. V. Costache, S. Auffret, S. Bandiera, B. Rodmacq, A. Schuhl and P. Gambardella, Nature **476**, 189 (2011).

[3] L. Liu, O. J. Lee, T. J. Gudmundsen, D. C. Ralph and R. A. Buhrman, Physical Review Letters **109** (9), 096602 (2012).

[4] C.-F. Pai, L. Liu, Y. Li, H. W. Tseng, D. C. Ralph and R. A. Buhrman, Applied Physics Letters **101** (12), 122404 (2012).

[5] C.-F. Pai, Y. Ou, L. H. Vilela-Leão, D. C. Ralph and R. A. Buhrman, Physical Review B **92** (6), 064426 (2015).

[6] X. Zhang, C. H. Wan, Z. H. Yuan, Q. T. Zhang, H. Wu, L. Huang, W. J. Kong, C. Fang, U. Khan and X. F. Han, Physical Review B **94** (17), 174434 (2016).

[7] X. Wang, C. Wan, W. Kong, X. Zhang, Y. Xing, C. Fang, B. Tao, W. Yang, L. Huang, H. Wu, M. Irfan and X. Han, Advanced Materials **30** (31), 1801318 (2018).

[8] D. Wu, G. Yu, Q. Shao, X. Li, H. Wu, K. L. Wong, Z. Zhang, X. Han, P. K. Amiri and K. L. Wang, Applied Physics Letters **108** (21), 212406 (2016).

[9] Y. Fan, P. Upadhyaya, X. Kou, M. Lang, S. Takei, Z. Wang, J. Tang, L. He, L.-T. Chang, M. Montazeri, G. Yu, W. Jiang, T. Nie, R. N. Schwartz, Y. Tserkovnyak and K. L. Wang, Nature Materials **13**, 699 (2014).

[10] K. Yasuda, A. Tsukazaki, R. Yoshimi, K. Kondou, K. S. Takahashi, Y. Otani, M. Kawasaki and Y. Tokura, Physical Review Letters **119** (13), 137204 (2017).

[11] Y. Fan, X. Kou, P. Upadhyaya, Q. Shao, L. Pan, M. Lang, X. Che, J. Tang, M. Montazeri, K. Murata, L.-T. Chang, M. Akyol, G. Yu, T. Nie, K. L. Wong, J. Liu, Y. Wang, Y. Tserkovnyak and K. L. Wang, Nature Nanotechnology **11**, 352 (2016).

[12] J. Han, A. Richardella, S. A. Siddiqui, J. Finley, N. Samarth and L. Liu, Physical Review Letters **119** (7), 077702 (2017).

[13] M. Dc, R. Grassi, J.-Y. Chen, M. Jamali, D. Reifsnyder Hickey, D. Zhang, Z. Zhao, H. Li, P. Quarterman, Y. Lv, M. Li, A. Manchon, K. A. Mkhoyan, T. Low and J.-P. Wang, Nature Materials **17** (9), 800-807 (2018).

[14] N. H. D. Khang, Y. Ueda and P. N. Hai, Nature Materials **17** (9), 808-813 (2018).

[15] Y. Wang, D. Zhu, Y. Wu, Y. Yang, J. Yu, R. Ramaswamy, R. Mishra, S. Shi, M. Elyasi, K.-L. Teo, Y. Wu and H. Yang, Nature Communications **8** (1), 1364 (2017).

[16] Y. Wang, P. Deorani, K. Banerjee, N. Koirala, M. Brahlek, S. Oh and H. Yang, Physical Review Letters **114** (25), 257202 (2015).

[17] A. R. Mellnik, J. S. Lee, A. Richardella, J. L. Grab, P. J. Mintun, M. H. Fischer, A. Vaezi, A. Manchon, E. A. Kim, N. Samarth and D. C. Ralph, Nature **511**, 449 (2014).

[18] Y. Liu, J. Besbas, Y. Wang, P. He, M. Chen, D. Zhu, Y. Wu, J. M. Lee, L. Wang, J. Moon, N. Koirala, S. Oh and H. Yang, Nature Communications **9** (1), 2492 (2018).

[19] Y. Zhang, K. He, C.-Z. Chang, C.-L. Song, L.-L. Wang, X. Chen, J.-F. Jia, Z. Fang, X. Dai, W.-Y. Shan, S.-Q. Shen, Q. Niu, X.-L. Qi, S.-C. Zhang, X.-C. Ma and Q.-K. Xue, Nature Physics **6**, 584 (2010).

[20] S. Shi, A. Wang, Y. Wang, R. Ramaswamy, L. Shen, J. Moon, D. Zhu, J. Yu, S. Oh, Y. Feng and H.

Yang, Physical Review B **97** (4), 041115 (2018).
[21] J. C. R. Sánchez, L. Vila, G. Desfonds, S. Gambarelli, J. P. Attané, J. M. De Teresa, C. Magén and A. Fert, Nature Communications **4**, 2944 (2013).
[22] D. Hsieh, Y. Xia, D. Qian, L. Wray, J. H. Dil, F. Meier, J. Osterwalder, L. Patthey, J. G. Checkelsky, N. P. Ong, A. V. Fedorov, H. Lin, A. Bansil, D. Grauer, Y. S. Hor, R. J. Cava and M. Z. Hasan, Nature **460**, 1101 (2009).
[23] Z. H. Pan, E. Vescovo, A. V. Fedorov, D. Gardner, Y. S. Lee, S. Chu, G. D. Gu and T. Valla, Physical Review Letters **106** (25), 257004 (2011).
[24] C. H. Li, O. M. J. van 't Erve, J. T. Robinson, Y. Liu, L. Li and B. T. Jonker, Nature Nanotechnology **9**, 218 (2014).
[25] G. Yu, P. Upadhyaya, Y. Fan, J. G. Alzate, W. Jiang, K. L. Wong, S. Takei, S. A. Bender, L.-T. Chang, Y. Jiang, M. Lang, J. Tang, Y. Wang, Y. Tserkovnyak, P. K. Amiri and K. L. Wang, Nature Nanotechnology **9**, 548 (2014).
[26] O. J. Lee, L. Q. Liu, C. F. Pai, Y. Li, H. W. Tseng, P. G. Gowtham, J. P. Park, D. C. Ralph and R. A. Buhrman, Physical Review B **89** (2), 024418 (2014).
[27] S. Emori, U. Bauer, S.-M. Ahn, E. Martinez and G. S. D. Beach, Nature Materials **12**, 611 (2013).
[28] C. Du, H. Wang, F. Yang and P. C. Hammel, Physical Review B **90** (14), 140407 (2014).
[29] W. Zhang, W. Han, X. Jiang, S.-H. Yang and S. S. P. Parkin, Nature Physics **11**, 496 (2015).
[30] See Supplemental Material [url] for the experimental methods, magnetic properties, SOT switching and harmonic Hall measurements in (W, Pt)/Ti/CoFeB/MgO structures, Optical MOKE method to obtain χ_{SOT}, temperature dependence and TI thickness dependence of SOT, which includes Refs. [31-32].
[31] M. Montazeri, P. Upadhyaya, M. C. Onbasli, G. Yu, K. L. Wong, M. Lang, Y. Fan, X. Li, P. Khalili Amiri, R. N. Schwartz, C. A. Ross and K. L. Wang, Nature Communications **6**, 8958 (2015).
[32] X. Fan, H. Celik, J. Wu, C. Ni, K.-J. Lee, V. O. Lorenz and J. Q. Xiao, Nature Communications **5**, 3042 (2014).
[33] Q. Hao and G. Xiao, Physical Review Applied **3** (3), 034009 (2015).
[34] M. Hayashi, J. Kim, M. Yamanouchi and H. Ohno, Physical Review B **89** (14), 144425 (2014).
[35] Q. Shao, G. Yu, Y.-W. Lan, Y. Shi, M.-Y. Li, C. Zheng, X. Zhu, L.-J. Li, P. K. Amiri and K. L. Wang, Nano Letters **16** (12), 7514-7520 (2016).
[36] S. Cho and B.-G. Park, Current Applied Physics **15** (8), 902-905 (2015).
[37] G. E. W. Bauer, E. Saitoh and B. J. van Wees, Nature Materials **11**, 391 (2012).
[38] C. O. Avci, K. Garello, M. Gabureac, A. Ghosh, A. Fuhrer, S. F. Alvarado and P. Gambardella, Physical Review B **90** (22), 224427 (2014).
[39] P. He, S. S. L. Zhang, D. Zhu, Y. Liu, Y. Wang, J. Yu, G. Vignale and H. Yang, Nature Physics **14** (5), 495-499 (2018).
[40] K. Park, J. J. Heremans, V. W. Scarola and D. Minic, Physical Review Letters **105** (18), 186801 (2010).
[41] H. L. Wang, C. H. Du, Y. Pu, R. Adur, P. C. Hammel and F. Y. Yang, Physical Review Letters **112** (19), 197201 (2014).
[42] J. Zhang, J. P. Velev, X. Dang and E. Y. Tsymbal, Physical Review B **94** (1), 014435 (2016).
[43] C.-Z. Chang, J. Zhang, X. Feng, J. Shen, Z. Zhang, M. Guo, K. Li, Y. Ou, P. Wei, L.-L. Wang, Z.-Q. Ji, Y. Feng, S. Ji, X. Chen, J. Jia, X. Dai, Z. Fang, S.-C. Zhang, K. He, Y. Wang, L. Lu, X.-C. Ma and Q.-K. Xue, Science **340** (6129), 167-170 (2013).

[44] A. J. Bestwick, E. J. Fox, X. Kou, L. Pan, K. L. Wang and D. Goldhaber-Gordon, Physical Review Letters **114** (18), 187201 (2015).
[45] K. Kondou, R. Yoshimi, A. Tsukazaki, Y. Fukuma, J. Matsuno, K. S. Takahashi, M. Kawasaki, Y. Tokura and Y. Otani, Nature Physics **12**, 1027 (2016).
[46] J. Zhang, C.-Z. Chang, Z. Zhang, J. Wen, X. Feng, K. Li, M. Liu, K. He, L. Wang, X. Chen, Q.-K. Xue, X. Ma and Y. Wang, Nature Communications **2**, 574 (2011).